Fast multicolor 3D imaging using aberration-corrected multifocus microscopy

Sara Abrahamsson[1–3], Jiji Chen[4,16], Bassam Hajj[4,16], Sjoerd Stallinga[5], Alexander Y Katsov[3], Jan Wisniewski[4,6], Gaku Mizuguchi[2,4,6], Pierre Soule[7], Florian Mueller[7,8], Claire Dugast Darzacq[4,7,9], Xavier Darzacq[4,7], Carl Wu[2,4,5], Cornelia I Bargmann[3,10], David A Agard[11,12], Maxime Dahan[4,13,14] & Mats G L Gustafsson[2,15]

Conventional acquisition of three-dimensional (3D) microscopy data requires sequential *z* scanning and is often too slow to capture biological events. We report an aberration-corrected multifocus microscopy method capable of producing an instant focal stack of nine 2D images. Appended to an epifluorescence microscope, the multifocus system enables high-resolution 3D imaging in multiple colors with single-molecule sensitivity, at speeds limited by the camera readout time of a single image.

© 2013 Nature America, Inc. All rights reserved.

Fast and sensitive acquisition of 3D data is one of the main challenges in modern biological microscopy. Most imaging modalities, such as wide-field, laser-scanning confocal, spinning-disk confocal and light-sheet microscopy[1], record information from one focal plane at a time. 3D images are assembled from a focal stack of 2D images acquired using sequential refocusing. This process is time consuming and can yield ambiguous spatio-temporal information because the focal planes are not recorded simultaneously. Moreover, the fast movement of the microscope stage (or objective) during refocusing can mechanically perturb the sample when an immersion objective is used (though this can be avoided by remote focusing[2]). Fluorescent probes can also be excited and photobleached while they are out of focus, which results in wasted photons and information.

To overcome these limitations, multifocus imaging forms an entire 3D focal stack that can be recorded in a single exposure of the camera, leaving only signal strength and camera frame rate to limit acquisition speed. Multifocus imaging has been applied in fluorescence microscopy using beam splitters to image up to four focal planes on separate cameras[3]. This method provides excellent light efficiency and a large lateral field of view corresponding to the entire surface area of the camera chip. However, refocusing by translating the camera away from the nominal focal plane induces spherical aberration after a refocus of a few microns[2]. It should also be noted that in the current configuration, this approach requires one camera per focal plane.

Here we report an aberration-corrected multifocus microscopy (MFM) method, which produces an instant focal stack of high-resolution 2D images simultaneously displayed on a single camera (**Fig. 1a–c**). It is based on the use of a diffractive grating to form multiple focus-shifted images[4,5] and on aberration-free refocusing[2]. Our system was designed with the following considerations: (i) sensitivity must be optimized to minimize photobleaching and phototoxicity and to enable high-speed imaging of weakly fluorescent samples such as single fluorophores; (ii) multiple focal planes must be acquired without aberrations, especially the dominating depth-induced spherical aberration, to avoid loss in resolution and contrast; (iii) the system must be corrected for the chromatic dispersion that arises when a diffractive element is used to image non-monochromatic light.

Our multifocus microscope consists of three specially designed optical elements (**Fig. 1d**) appended to the camera port of a standard, high-resolution epifluorescence microscope. Two relay lenses are also used, to form a secondary pupil plane (Fourier plane) and the final image plane (**Fig. 1a**). The diffractive multifocus grating (MFG) is placed in the Fourier plane to form the multifocus image, and it is followed by the chromatic correction grating (CCG) and prism. The MFG performs two distinct functions. First, it splits the fluorescence light emitted from the sample into separate paths, thus forming an array of $N \times N$ images of the sample on the camera. Each image corresponds to a 2D diffractive order (m_x, m_y) of the grating. Here we describe an MFG with nine focal planes, which are formed by the central 3×3 diffractive orders m_x, $m_y = 0, \pm 1$. To minimize light loss, we use a phase-only grating of fused silica, with a grating function (**Fig. 1d**) designed to distribute the sample emission light evenly and efficiently among the nine focal planes. At the design wavelength (515 nm), the measured efficiency of our MFG (custom made by Creative Microsystems) is ~65% with even distribution between images, as illustrated in **Supplementary Figure 1**. This is close

[1]Joint Graduate Group in Bioengineering, University of California, San Francisco (UCSF)/University of California, Berkeley, San Francisco, California, USA. [2]Howard Hughes Medical Institute, Janelia Farm Research Campus, Ashburn, Virginia, USA. [3]Laboratory for Neural Circuits and Behavior, The Rockefeller University, New York, New York, USA. [4]Transcription Imaging Consortium, HHMI, Janelia Farm Research Campus, Ashburn, Virginia, USA. [5]Department of Imaging Science and Technology, Delft University of Technology, Delft, The Netherlands. [6]Laboratory of Biochemistry and Molecular Biology, National Cancer Institute, Bethesda, Maryland, USA. [7]Functional Imaging of Transcription, Institut de Biologie de l'École Normale Supérieure, Centre National de la Recherche Scientifique (CNRS) Unité Mixte de Recherche (UMR) 8197, Paris, France. [8]Institut Pasteur, Imaging and Modeling Group, CNRS, Unité de Recherche Associée 2582, Paris, France. [9]Université Paris Diderot, Paris, France. [10]Howard Hughes Medical Institute (HHMI), The Rockefeller University, New York, New York, USA. [11]HHMI, UCSF, San Francisco, California, USA. [12]Department of Biochemistry & Biophysics, UCSF, San Francisco, California, USA. [13]Laboratoire Kastler Brossel, CNRS UMR 8552, Institut de Biologie et Département de Physique, École Normale Supérieure, Paris, France. [14]Present address: Institut Curie, CNRS UMR 168, Paris, France. [15]Deceased. [16]These authors contributed equally to this work. Correspondence should be addressed to S.A. (sara.abrahamsson@gmail.com) or M.D. (maxime.dahan@curie.fr).

RECEIVED 14 MAY; ACCEPTED 22 OCTOBER; PUBLISHED ONLINE 9 DECEMBER 2012; DOI:10.1038/NMETH.2277

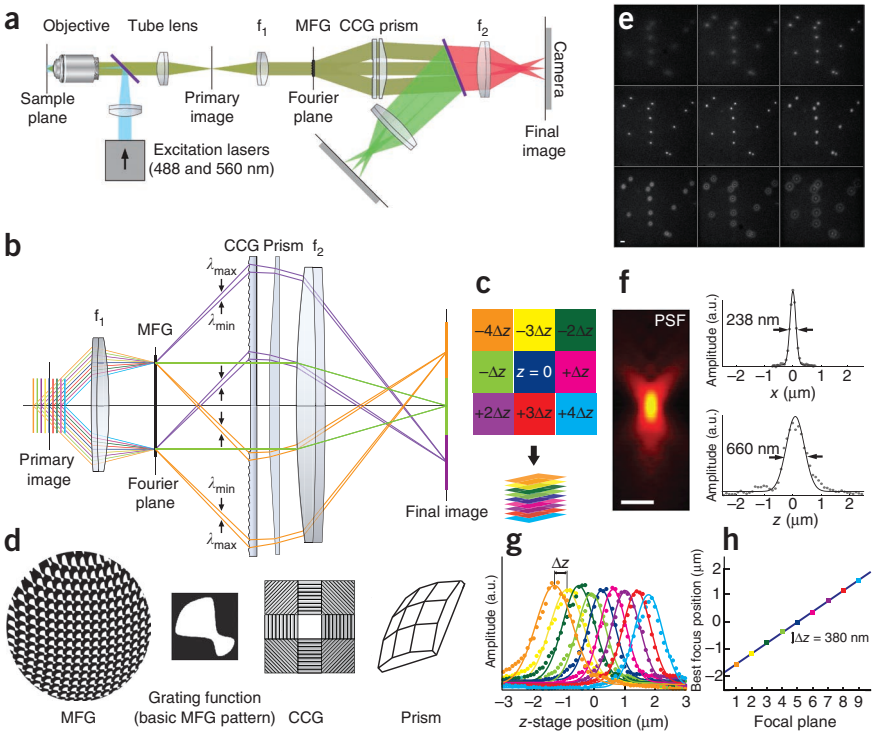

Figure 1 | Aberration-corrected multifocus microscopy (MFM). (**a**) Multifocus optical elements are appended to a wide-field fluorescence microscope after the primary image plane (at the camera port). Two relay lenses (f_1 and f_2, first and second relay lens, with focal lengths f_1 = 150 and f_2 = 200 mm) create a conjugate pupil plane (Fourier plane) and the final image plane. The multifocus grating (MFG) is placed in the Fourier plane and followed by the chromatic correction grating (CCG) and prism. A dichroic mirror (purple) splits the color channels onto separate cameras. (**b**) The MFG splits and shifts the focus of the sample emission light to form an instant focal series, in which each focal plane corresponds to a diffractive order of the MFG. Ray colors denote individual focal planes (diffractive orders). The CCG and prism correct the chromatic dispersion, illustrated by rays of wavelengths λ_{max} and λ_{min}, introduced by the MFG. (**c**) The instant focal stack recorded on the camera is computationally assembled into a 3D volume. (**d**) Schematics of the MFG, a phase-only diffractive grating with etch depth π; the grating function (basic grating pattern) of the MFG, optimized to distribute light evenly into the central 3 × 3 diffractive orders that form the nine focal planes; the CCG, with panels containing blazed diffractive gratings that reverse the dispersion of the MFG (central panel is blank); and the prism, which directs the images to their positions on the camera. Note the geometrical distortion of the MFG pattern, which introduces a phase shift that is dependent on diffractive order (m_x, m_y) and gives rise to the focus shift in each plane of the multifocus image. (**e**) Raw, multifocus image of 200-nm fluorescent beads. As illustrated in **c**, the central tile is the (nondiffracted) traditional microscope image of the nominal focal plane. The surrounding eight tiles are the duplicate focus-shifted images, formed by diffraction in the MFG. The focus step between successive planes is Δz = 380 nm. (**f**) Axial (xz) point-spread function (PSF), radially averaged and displayed in log scale. (**g**) Gaussian curves fitted to the bead signal of each plane at different z positions of the stage. Best focus position is estimated as the maximum of the fitted curve (**Supplementary Video 1**). (**h**) Plot of the best focus position of each plane. The linear curve verifies the constant focus step Δz between planes. Scale bars, 1 μm.

© 2013 Nature America, Inc. All rights reserved.

to the theoretical maximum efficiency (~67%) of this type of grating, but it could be improved (theoretically to ~93%) by using a multiphase element[6]. To implement an MFM microscope with more focal planes, one would use a different MFG to image the m_x, $m_y = 0, \pm1, \pm2$ diffractive orders, obtaining 5 × 5 = 25 planes, as shown in **Supplementary Figure 1**.

The second function of the MFG is to refocus the array of images so that it forms an instant focal series with a constant focus step Δz. When refocusing deep into a thick sample, the microscope objective is used at a focal distance for which it is not designed. This normally gives rise to depth-induced spherical aberration, which deteriorates the image[2]. To avoid this problem, we have used the Abbe sine condition[7] to calculate the defocus phase error $\delta\phi(z)$ in the Fourier plane of a point source at defocus z in the sample. We let the MFG apply an equal but opposite phase shift that entirely reverses the out-of-focus wavefront error (Online Methods). Light from the out-of-focus plane thus exits the MFG with a flat wavefront, as illustrated in **Supplementary Figure 2**, and is properly focused onto the camera. The phase shift is introduced by a carefully calculated geometrical distortion of the MFG pattern (**Fig. 1d**) and is dependent on diffractive order so that each duplicate image in the $N \times N$ array obtains a focus shift $\Delta z \times (m_x + N \times m_y)$ (**Fig. 1c**). The magnitude of the MFG distortion determines the step size Δz. To adapt the

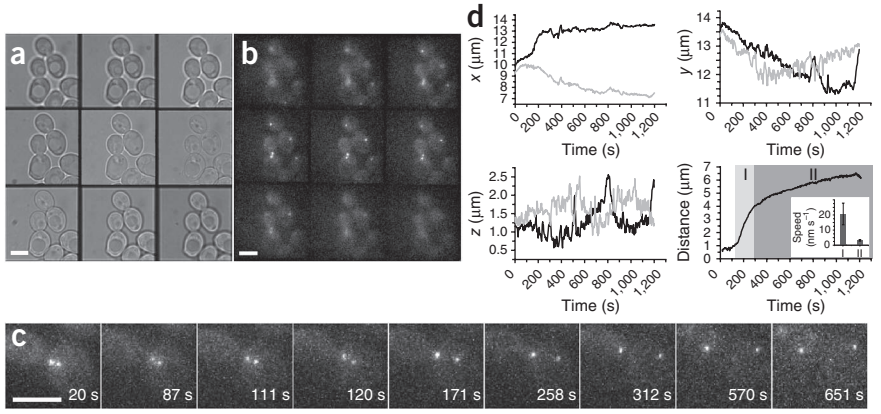

Figure 2 | Multifocus imaging of yeast centromeres. (**a**,**b**) Multifocus transmission (**a**) and fluorescence (**b**) images of *S. cerevisiae* expressing Cse4-GFP. (**c**) Separation of the centromeres during anaphase over time (maximum-intensity projections). (**d**) Movement in 3D of the two centromere clusters (black and gray). Bottom right, separation between the centromere clusters over time. Rapid movement (phase I) is followed by slow movement (phase II). Inset, average speed during phases I and II (n = 5 cells). Scale bars, 5 μm.

microscope to a variety of samples and imaging applications, we have designed several gratings, which produce different focus shifts ranging from 250 nm to 2 µm, spanning 2.25–18 µm of sample depth per 3D image.

The MFG is in itself sufficient for imaging monochromatic light. However, even across the relatively narrow (~30-nm) wavelength spectrum of a single fluorophore, chromatic dispersion—inherent to any diffractive element[7]—severely deteriorates resolution. To correct the dispersion, we have designed the CCG (custom made by Tessera), which is placed after the MFG at a position where the diffractive orders are separated (**Fig. 1b**). The CCG panels consist of blazed transmission gratings (oriented as shown in **Fig. 1d**) that reverse the dispersion from the MFG (Online Methods). On its own, the CCG would not only remove the chromatic dispersion but, unfortunately, also reverse the image separation obtained by the MFG. Therefore, we have added a multifaceted refractive prism (custom made by Rocky Mountain Instruments) to direct the diffractive orders to their positions on the camera. The CCG spacing is adjusted to compensate for the additional dispersion of the prism. (The optical properties of the CCG and prism are illustrated in **Supplementary Fig. 3**.) We hereby obtain an essentially diffraction-limited point-spread function (PSF) for fluorophores across the visible spectrum. For an MFG with Δz = 380 nm and using a 100× Nikon oil-objective (numerical aperture (NA) = 1.4), the full width at half maximum of the PSF is 238 nm laterally and 660 nm axially (**Fig. 1e**,**f** and **Supplementary Videos 1** and **2**). The focus shift between planes is verified in **Figure 1g**,**h** and further discussed in **Supplementary Note 1**.

To evaluate the performance of our MFM in living samples, we imaged *Saccharomyces cerevisiae* (**Fig. 2**) expressing Cse4-GFP, a histone H3 variant that binds to centromeric DNA (**Supplementary Note 2**). We were able to track the centromeres (each labeled by 30–80 fluorescent molecules[8,9]) in three dimensions and observe their behavior during cell division[10] with one image (covering a volume of 20 × 20 × 3.5 µm^3) recorded every 3 s (exposure time = 100 ms). We observed the biphasic behavior of centromeres during cell division (**Supplementary Videos 3** and **4**), with a fast initial separation speed of 20 nm s^{-1} over ~2 min followed by a slower separation of 3 nm s^{-1} over ~15 min.

High sensitivity and spatiotemporal resolution are paramount in single-molecule imaging, in which the acquisition of 3D data is a major challenge[11]. In a single-particle tracking experiment, we imaged RNA polymerase II (labeled using HaloTag (Promega)) in the nucleus of a human osteosarcoma cell line[12] (**Supplementary Note 3**). We were able to image the heterogeneous nuclear mobility of RNA polymerase II in three dimensions at 35 frames per s, observing bound and mobile states and transitions between them (**Fig. 3** and **Supplementary Videos 5** and **6**). The depth (~4 µm) over which we could detect and reconstruct individual trajectories in MFM compares well to other 3D single-fluorophore localization techniques: ~3 µm for double-helix[13], ~1 µm for astigmatic[14] and ~2 µm for biplane[15] imaging.

We also explored MFM of thicker samples with a larger imaging volume of 60 × 60 × 18 µm^3, at lower magnification and coarser focal plane separation Δz = 2 µm, to visualize fluorescently labeled neurons in the developing *Caenorhabditis elegans* embryo (**Supplementary Note 4**). At nine volumes per second, we were able to image the entire late embryo moving rapidly

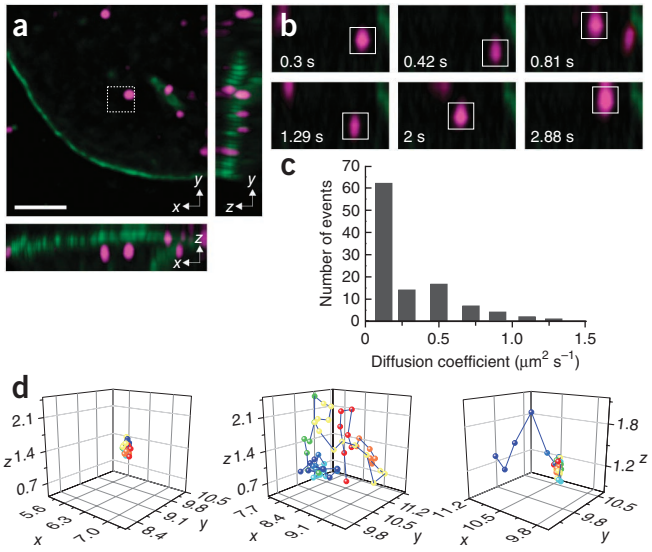

Figure 3 | Single-molecule tracking of RNA polymerase II. (**a**) Maximum-intensity projection (MIP) of the 3D volume of the first frame of **Supplementary Video 5** on the indicated planes. Purple spots correspond to single Halo-tagged RNA polymerase II molecules in U2OS cells. The nuclear membrane (green) is visualized using lamin B1–GFP. Scale bar, 5 µm. (**b**) Movement of the single molecule marked by the dashed frame in **a**, visualized in MIP in the *xz* plane (scale as in **a**). (**c**) Histogram of diffusion coefficient (n = 109 molecules from seven cells). (**d**) Examples of individual trajectories of RNA polymerase II, showing (left to right) a bound molecule, a diffusing molecule and a molecule with mixed dynamics. Dimensions are in micrometers. Corresponding 3D temporal sequences are available in **Supplementary Video 6**.

inside the eggshell (**Supplementary Videos 7** and **8**), a stage previously inaccessible to full-volume imaging[16].

In summary, we have implemented an aberration-corrected multifocus imaging system for fast 3D imaging. Simultaneous acquisition of all focal planes eliminates the spatiotemporal ambiguity of sequentially recorded z stacks. The resolution of the multifocus image is that of the wide-field microscope to which it is appended, and the imaging sensitivity (light efficiency) is currently ~60% of that of the wide-field fluorescence microscope. Field of view and acquisition rate are determined by camera chip size and readout speed. Thanks to its ease of use, compatibility with standard microscopes and excellent imaging performance, MFM should facilitate the rapid acquisition of 3D data from the level of single molecules up to that of small organisms.

METHODS

Methods and any associated references are available in the online version of the paper.

Note: Supplementary information is available in the online version of the paper.

ACKNOWLEDGMENTS

We dedicate this paper to the late Mats Gustafsson. We thank K. Wicker, R. Heinzmann, T. Wilson and D. Grunwald for valuable discussions about multifocus microscopy; C. Zimmer for his help with the 3D localization algorithm; F. Amat and A. Verma for assistance with data processing; L. Shao, L. Winoto, J. Sedat, R. Singer and E. Betzig for discussions on 3D microscopy; V. Iyer for discussions on hardware control; Z. Zhang and Y. Li (HHMI Janelia Farm) for sharing reagents; H. White and H. Rego for assistance in live-cell imaging; and V. Butler and R. Kerr (HHMI Janelia Farm) and W. Schafer (MRC Laboratory of Molecular Biology) for the *C. elegans* strain. S.A. would like to thank G. Rubin, K. Moses and R. Tijan for

© 2013 Nature America, Inc. All rights reserved.

ensuring continued funding for this project during and after the difficult time of M.G.'s sickness. A.Y.K. is supported by a Jane Coffin Childs postdoctoral fellowship. M.D. acknowledges the support of a Fulbright fellowship. X.D. and M.D. are supported by grant ANR-08-PCVI-0013 from Agence Nationale pour la Recherche. D.A.A. is supported by US National Institutes of Health grant GM31627. S.A., C.I.B. and D.A.A. are supported by the HHMI. J.W., G.M. and C.W. are supported by the Center for Cancer Research, National Cancer Institute and HHMI.

AUTHOR CONTRIBUTIONS

The optical layout was conceived by M.G.L.G. Optical design and optimizations were made by M.G.L.G. and S.A. S.A. built the system and implemented the hardware control electronics. J.C., B.H. and M.D. performed single-molecule and yeast experiments. S.A., B.H., J.C. and M.D. developed image processing tools, and B.H. and J.C. analyzed the data. S.A. and A.Y.K. acquired the *C. elegans* data. J.W. and G.M. constructed the yeast strain; J.W. and C.W. participated in centromere imaging. P.S., C.D.D. and X.D. constructed and characterized the RPB1 cellular system. S.S. contributed to the theoretical performance evaluation of the microscope. F.M. and X.D. provided the 3D single-emitter detection algorithm. M.G.L.G., D.A.A. and C.I.B. supervised the project. S.A. and M.D. prepared the manuscript.

COMPETING FINANCIAL INTERESTS

The authors declare no competing financial interests.

Published online at http://www.nature.com/doifinder/10.1038/nmeth.2277. Reprints and permissions information is available online at http://www.nature.com/reprints/index.html.

1. Fischer, R.S., Wu, Y., Kanchanawong, P., Shroff, H. & Waterman, C.M. *Trends Cell Biol.* **21**, 682–691 (2011).
2. Botcherby, E.J., Juskaitis, R., Booth, M.J. & Wilson, T. *Opt. Lett.* **32**, 2007–2009 (2007).
3. Prabhat, P., Ram, S., Ward, E.S. & Ober, R.J. *IEEE Trans. Nanobioscience* **3**, 237–242 (2004).
4. Blanchard, P.M. & Greenaway, A.H. *Appl. Opt.* **38**, 6692–6699 (1999).
5. Blanchard, P.M. & Greenaway, A.H. *Opt. Commun.* **183**, 29–36 (2000).
6. Mait, J.N. *J. Opt. Soc. Am. A Opt. Image Sci. Vis.* **12**, 2145–2158 (1995).
7. Born, M. & Wolf, E. *Principles of Optics* (Cambridge University Press, 1999).
8. Lawrimore, J., Bloom, K.S. & Salmon, E.D. *J. Cell Biol.* **195**, 573–582 (2011).
9. Coffman, V.C., Wu, P., Parthun, M.R. & Wu, J.Q. *J. Cell Biol.* **195**, 563–572 (2011).
10. Pearson, C.G., Maddox, P.S., Salmon, E.D. & Bloom, K. *J. Cell Biol.* **152**, 1255–1266 (2001).
11. Pinaud, F., Clarke, S., Sittner, A. & Dahan, M. *Nat. Methods* **7**, 275–285 (2010).
12. Darzacq, X. *et al. Nat. Struct. Mol. Biol.* **14**, 796–806 (2007).
13. Pavani, S.R. *et al. Proc. Natl. Acad. Sci. USA* **106**, 2995–2999 (2009).
14. Huang, B., Wang, W., Bates, M. & Zhuang, X. *Science* **319**, 810–813 (2008).
15. Ram, S., Prabhat, P., Chao, J., Ward, E.S. & Ober, R.J. *Biophys. J.* **95**, 6025–6043 (2008).
16. Wu, Y. *et al. Proc. Natl. Acad. Sci. USA* **108**, 17708–17713 (2011).

© 2013 Nature America, Inc. All rights reserved.

ONLINE METHODS

Design of the MFG grating function. In a phase-only diffractive grating, the shape of the grating pattern and its etch depth constitute the grating function and determine the energy distribution between diffractive orders. To optimize light efficiency in MFM, we wished to direct the fluorescence emission light from the sample with maximum efficiency into the orders we chose to image. Furthermore, light should be distributed evenly between these orders so that one can use minimal exposure time to record each multifocus image while still getting sufficient signal in each plane and to obtain an even signal throughout the 3D image.

The amplitude point-spread function (PSF) of an imaging system can be calculated as the square of the Fourier transform of the pupil function[17,18]. In MFM the pupil function is modified by the phase shift of the MFG, which we can model with a matrix G. The altered PSF of an aberration-free microscope in which the MFG is inserted in the Fourier plane is then given by the square of the Fourier transform of the matrix G. We have used this property to optimize the grating function (**Fig. 1d**) as described below. (Similar algorithms have been used before to tailor the PSF of imaging systems[17].)

We create a matrix T as the target function representing the multifocus PSF we desire. For a system with nine planes, the desired PSF consists of 3×3 points of maximum brightness and evenness. A starting guess for the phase grating G is made in the form of a matrix of randomly distributed black (−1) and white (+1) pixels representing phase shifts 0 and π, respectively. The matrix G is Fourier transformed using the command fft2 (which executes a fast 2D Fourier transform[18]), yielding the complex-valued PSF*, which is squared to yield the real-valued amplitude PSF[7]. The algorithm now randomly selects a pixel in G and flips it to the opposite phase. This matrix is Fourier transformed, yielding a new PSF. The two PSFs are compared to the target function T, and the pattern that gives a PSF with a better resemblance to T is kept as the new matrix G. The algorithm steps through all the pixels in G in a randomized fashion and flips them if this gives better resemblance to the target function. It terminates when it has reached a local minimum: when no pixels are flipped during a round of stepping through all the pixels of the matrix. The algorithm is thus not guaranteed to converge to an optimal solution; rather, it requires some trial and error from the user to find a good pattern. Using this algorithm, we arrived at a pattern that produces a PSF of $3 \times 3 = 9$ points. A similar pattern was previously described as an example of an optimally efficient pattern for this type of grating[6]. Calculated efficiency of our version of the MFG pattern was 67%, and measured efficiency of our MFG based on this pattern was found to be 65%, with evenness between focal planes. We also created a pattern producing $5 \times 5 = 25$ points with an efficiency of 78%. Grating functions and PSFs are illustrated in **Supplementary Figure 1**.

Aberration-corrected refocusing. In a standard wide-field microscope, the nominal focal plane of the sample ($z = 0$) is conjugated, via the objective and the tube lens, to the plane of the camera. The principle of MFM is to simultaneously focus the light originating from the in-focus plane and a set of out-of-focus planes onto the camera, thereby forming an instant focal series (the multifocus image). Light from a point source in the nominal focal plane has a flat wavefront in Fourier space, whereas wavefronts from defocused sources have a curvature, the defocus wavefront error $\delta\phi(z)$ (**Supplementary Fig. 2a**). To form an image in the nominal focal plane of the out-of-focus source, it is necessary to reverse this wavefront error so that the out-of-focus wavefront is flat before it hits the final focusing lens. This task is performed by the MFG, positioned in the secondary Fourier plane. The primary Fourier plane is the objective pupil plane, which is situated inside the objective itself. We therefore use the tube lens and first relay lens, f_1, to form a secondary Fourier plane, conjugate to the objective pupil (**Fig. 1a**).

We start by computing, for each point (x_p, y_p) in the pupil plane, the out-of-focus phase error $\delta\phi(z)$ of the wavefront from a point source located on the optical axis in a plane at defocus z from the nominal focal plane[2]. We let $r_p = \sqrt{(x_p^2 + y_p^2)}$ denote the radial coordinate position in the pupil and $\rho = r_p/R_p$ the normalized radial coordinate, where $R_p = \mathrm{NA} \times f_{obj}$ is the pupil radius and f_{obj} is the focal length of the objective. The numerical aperture is defined as $\mathrm{NA} = n \times \sin(\alpha)$, where n is the diffractive index of the objective immersion medium (and sample) and α is the highest incident-ray angle collected by the objective. We also use the free-space wave number $k = 2\pi/\lambda$ (λ is the sample fluorescence emission wavelength). As illustrated in **Supplementary Figure 2b**, assuming radial symmetry and using polar coordinates, we calculate the defocus phase error of a ray entering the objective at an angle θ ($\theta \le \alpha$) as

$$\delta\phi(z) = n \times k \times z \times \cos(\theta) = n \times k \times z \times \sqrt{1 - \sin^2(\theta)}$$

Using the Abbe sine condition, which states that $\rho = \sin(\theta)/\sin(\alpha)$, we can relate the angle θ to radial position r_p in the pupil plane. We use this relation to write

$$\sin^2(\theta) = \rho^2 \times \sin^2(\alpha) = (r_p / R_p)^2 \times R_p^2/(n \times f_{obj})^2 = r_p^2/(n \times f_{obj})^2 = (x_p^2 + y_p^2)/(n \times f_{obj})^2$$

Here we have gotten rid of the radial symmetry (to introduce the distortion in x and y individually) by returning to Cartesian coordinates. We can now write the equation for the defocus phase error for a plane at defocus z at every point (x_p, y_p) in the pupil

$$\delta\phi(z) = n \times k \times z \times \sqrt{1 - (x_p^2 + y_p^2)/(n \times f_{obj})^2}$$

A geometrical distortion δx of a periodic grating pattern (with spacing d) in the pupil plane introduces a phase shift $\delta\phi$ in the diffracted wavefront, which is dependent on the diffractive order m_x according to

$$\delta\phi_{m_x}(\delta x) = 2\pi \times (\delta x / d) \times m_x$$

To create a multifocus image consisting of $N \times N$ planes with a constant focus step Δz, we impose a local distortion of the MFG grating pattern. (The distortion is applied to a periodic pattern with spacing d of the grating function in **Fig. 1d**.) To create a proper refocus, the distortion is applied stronger by a factor N in one direction

$$\delta x(x_p, y_p) = (d/2\pi) \times n \times k \times z \times \sqrt{1 - (x_p^2 + y_p^2)/(n \times f_{obj})^2}$$
$$\delta y(x_p, y_p) = N \times \delta x(x_p, y_p)$$

© 2013 Nature America, Inc. All rights reserved.

doi:10.1038/nmeth.2277

This gives us a total focus shift in each diffractive order (m_x, m_y) of $\Delta z \times (m_x + N \times m_y)$. For example, with $N = 3$, the order $(m_x, m_y) = (+1, +1)$ gets focus shifted by $\Delta z \times (1 + 3 \times 1) = \Delta z \times 4$ and the zeroth order (0, 0) gets no focus shift.

Chromatic correction. After the MFG, each horizontal and vertical diffractive order has a dispersion $\delta\lambda/d$ (where d is the average grating period of the MFG pattern, and $\delta\lambda$ is the wavelength bandwidth imaged). Each diagonal order has a dispersion $\sqrt{2} \times \delta\lambda / d$ due to geometry. If left uncorrected the dispersion would give rise to a severe outward smear in the image (**Supplementary Fig. 3a**). The CCG is placed at a distance from the MFG so that each order goes through its own designated panel. In the individual blazed grating panels, >95% of the energy is distributed into the −1 (minus one) diffractive order (**Supplementary Fig. 3b**). To reverse the MFG dispersion, the CCG should therefore have a period equal to that of the MFG ($d_{CCG} = d$). However, if used alone, the CCG would completely oppose the image-separating action of the MFG, and the diffractive orders would recombine to form a single image in the center of the sensor (**Supplementary Fig. 3c**). We have therefore added, after the CCG, a nine-faceted refractive prism, which maintains image separation by deflecting the orders while they are still separated (**Supplementary Fig. 3d**). The prism has a dispersive power $D_{prism} = (n_{silica} - 1) \times \xi$, where n_{silica} is the refractive index of the UV-grade fused silica prism and ξ is the prism angle[7]. The period of the CCG is therefore adjusted by d_p to also remove the effect of the dispersive power of the prism, so that $d_{CCG} = d + d_p$ in the side panels and $\sqrt{2} \times d_{CCG}$ in the corner panels. The light efficiency of the chromatic correction module is determined by the efficiency of the blazed grating (better than 95%) and the transmittance of the (AR-coated) prism (also better than 95%). In summary, we have designed a chromatic correction scheme which is effective, light efficient and easy to incorporate in a straight beam path between the MFG and the second relay lens, and which can be used to image fluorophores from the entire visible spectrum.

Data acquisition. Cells were illuminated in epifluorescence with laser light. For GFP excitation we used a 488-nm laser (488 Sapphire, Coherent) with intensity ~40–80 W cm^{-2}. For experiments with TMR dyes, we used a 561-nm laser (MPB Lasertech) of excitation intensity ~1 kW cm^{-2}. In both cases, we used a double-band dichroic mirror (Di01-R488/561, Semrock). We used a 100× Nikon oil-immersion objective with NA = 1.4 for yeast and RNA polymerase imaging and a 60× Nikon water-immersion objective for *C. elegans* imaging. In the emission pathway, before the second relay lens, the fluorescent light was split onto two cameras using a dichroic mirror (custom made by Chroma Technology) with cutoff at 570 nm. Emission filters centered at 520 nm (FF01-520/35, Semrock) and 617 nm (FF01 617/70, Semrock) were placed in front of the cameras in the green and red channel, respectively. For all experiments we used back-illuminated EMCCD cameras (Andor Technology). For the yeast and RNA polymerase II imaging we used Ixon3-DU897E cameras, and for the *C. elegans* imaging we used the iXon-888 camera, which has lower readout speed but a larger chip size. Further descriptions of the biological imaging experiments are available in **Supplementary Notes 2**, **3** and **4**.

Data processing. To reconstruct the 3D imaging volume from the multifocus image, the nine focal planes were aligned on top of one another using calibration data obtained with 200-nm fluorescent beads (Invitrogen) mounted on a coverslip. We recorded a focal series by scanning the bead sample along the z axis using a piezoelectric stage (nanoX-200, PiezosystemJena) (**Fig. 1g**,**h**). During this process, the beads are successively focused in each of the nine subimages. We then performed a 2D Gaussian fit on the z projection of each focal plane to locate the beads in the different subimages. Using rotation, translation and stretching of the subimages, we determined a transformation matrix enabling the focal planes to be superimposed with an accuracy of ~10 nm. The transformation matrix was subsequently used on the biological data to reconstruct the 3D volume for each time frame. The calibration data were also used to estimate and correct the small differences in transmitted intensities between images. For 3D particle tracking we used the u-track algorithm[19] (an open-source, multiple-particle tracking software).

17. Neil, M.A., Wilson, T. & Juskaitis, R. *J. Microsc.* **197**, 219–223 (2000).
18. Goodman, J.W. *Introduction to Fourier Optics* (Roberts & Co., 2005).
19. Jaqaman, K. *et al. Nat. Methods* **5**, 695–702 (2008).

© 2013 Nature America, Inc. All rights reserved.